

Interface-driven chiral magnetism and current-driven domain walls in insulating magnetic garnets

Can Onur Avci, Ethan Rosenberg, Lucas Caretta, Felix Büttner , Maxwell Mann, Colin Marcus, David Bono, Caroline A. Ross and Geoffrey S. D. Beach *

Magnetic oxides exhibit rich fundamental physics^{1–4} and technologically desirable properties for spin-based memory, logic and signal transmission^{5–7}. Recently, spin-orbit-induced spin transport phenomena have been realized in insulating magnetic oxides by using proximate heavy metal layers such as platinum^{8–10}. In their metallic ferromagnet counterparts, such interfaces also give rise to a Dzyaloshinskii–Moriya interaction^{11–13} that can stabilize homochiral domain walls and skyrmions with efficient current-driven dynamics. However, chiral magnetism in centrosymmetric oxides has not yet been observed. Here we discover chiral magnetism that allows for pure spin-current-driven domain wall motion in the most ubiquitous class of magnetic oxides, ferrimagnetic iron garnets. We show that epitaxial rare-earth iron garnet films with perpendicular magnetic anisotropy exhibit homochiral Néel domain walls that can be propelled faster than 800 m s^{-1} by spin current from an adjacent platinum layer. We find that, despite the relatively small interfacial Dzyaloshinskii–Moriya interaction, very high velocities can be attained due to the antiferromagnetic spin dynamics associated with ferrimagnetic order.

Chiral exchange interactions arise from broken spatial inversion symmetry. Only a limited number of inversion-asymmetric bulk magnetic materials are known^{14–16}, but engineered interfaces can induce a chiral Dzyaloshinskii–Moriya interaction (DMI) in common centrosymmetric ferromagnets^{17–20} in which topological spin textures would otherwise not be found. So far, most research has focused on metallic ferromagnet/heavy-metal bilayers, in which chiral spin textures can be stabilized by an interfacial DMI at room temperature^{21–23}. Such systems simultaneously benefit from the large spin Hall effect present in DMI-inducing heavy metals like platinum, which provides a source of pure spin current to manipulate chiral spin textures efficiently^{21,24}.

Due to their chemical and structural complexity, magnetic oxides exhibit a broader range of exotic and useful properties than metals, and oxide-based spintronics may permit functionalities not otherwise readily achieved^{4,5,7}. Insulating magnetic oxides are of particular interest due to their low damping, large magnon diffusion length and the possibility to generate and transmit pure spin currents with minimal dissipation^{6,9}. However, the realization of chiral spin textures in magnetic oxides remains a challenge, as few bulk chiral magnetic oxides are known¹⁶. The interface-induced DMI in centrosymmetric oxides has so far only been studied in conducting oxides at cryogenic temperatures^{25–27} using indirect magneto-transport measurements, the interpretation of which can be ambiguous^{28,29}.

In this Letter we characterize pure spin-current-induced domain wall (DW) motion in insulating rare-earth iron garnet films capped by platinum, revealing an interfacial DMI at room temperature whose strength we quantitatively deduced from the dynamics. In our experiments we examined perpendicularly magnetized 5- to 7-nm-thick $\text{Tm}_3\text{Fe}_5\text{O}_{12}$ (TmIG) and $\text{Tb}_3\text{Fe}_5\text{O}_{12}$ (TbIG) films grown epitaxially on (111)-oriented $\text{Gd}_3\text{Ga}_5\text{O}_{12}$ substrate and covered by a 4-nm-thick Pt layer (see Methods). The DW motion was studied in lithographically patterned tracks (Fig. 1a) with contacts at either end for current injection and with an orthogonal Au wire for domain nucleation (see Methods). Lateral voltage contacts were included for Hall resistance measurements. Magnetization reversal was detected locally using a scanning magneto-optical Kerr effect (MOKE) polarimeter with a focused laser spot size of $\sim 5 \mu\text{m}$.

Figure 1 summarizes the magneto-transport and magnetic switching measurements used to characterize spin transport across the Pt/TmIG interface. Figure 1b presents the Hall resistance R_H versus in-plane field H oriented 45° from the injected current density j (see Methods). The $\sin^2\theta$ dependence arises from the spin Hall magnetoresistance (SMR)⁸, where θ is the azimuthal angle of the (normalized) magnetization vector \mathbf{m} , which rotates from out-of-plane to in-plane as H increases. From the amplitude change $\Delta R_H = R_{\text{SMR}} \cong 8.1 \text{ m}\Omega$ and the measured sheet resistance $R_\square = 75 \Omega$, we find an SMR ratio of $R_{\text{SMR}}/R_\square \cong 1.1 \times 10^{-4}$ indicative of a large spin-mixing conductance, similar to previous reports¹⁰. The imaginary part of the spin-mixing conductance leads to an additional anomalous Hall-like SMR contribution to R_H that tracks the out-of-plane magnetization¹⁰, as seen in the hysteresis loops in Fig. 1c. This contribution gives rise to the hysteretic behaviour around zero field in Fig. 1b, due to slight misalignment of H relative to the sample plane. Finally, Fig. 1d demonstrates spin Hall current-induced switching of the TmIG magnetization in the presence of a longitudinal field H_x detected by both Hall effect and MOKE measurements. The small switching current density implies a large damping-like torque reflecting the large spin Hall effect in the Pt layer combined with significant interfacial spin transparency. The damping-like torque effective field H_{DL} was quantified using harmonic measurements (see Supplementary Information), yielding an effective spin Hall angle $\theta_{\text{SH}}^{\text{eff}} \sim 2\%$, consistent with previous reports¹⁰.

Figure 2a shows time-resolved MOKE transients measured at several positions along the track in Fig. 1a during field (H_x)-driven motion of a DW initialized near the DW nucleation line (see Methods). The locally probed magnetization switching time increases linearly with increasing distance from the nucleation line (Fig. 2b), confirming reversal by a single propagating DW. The average

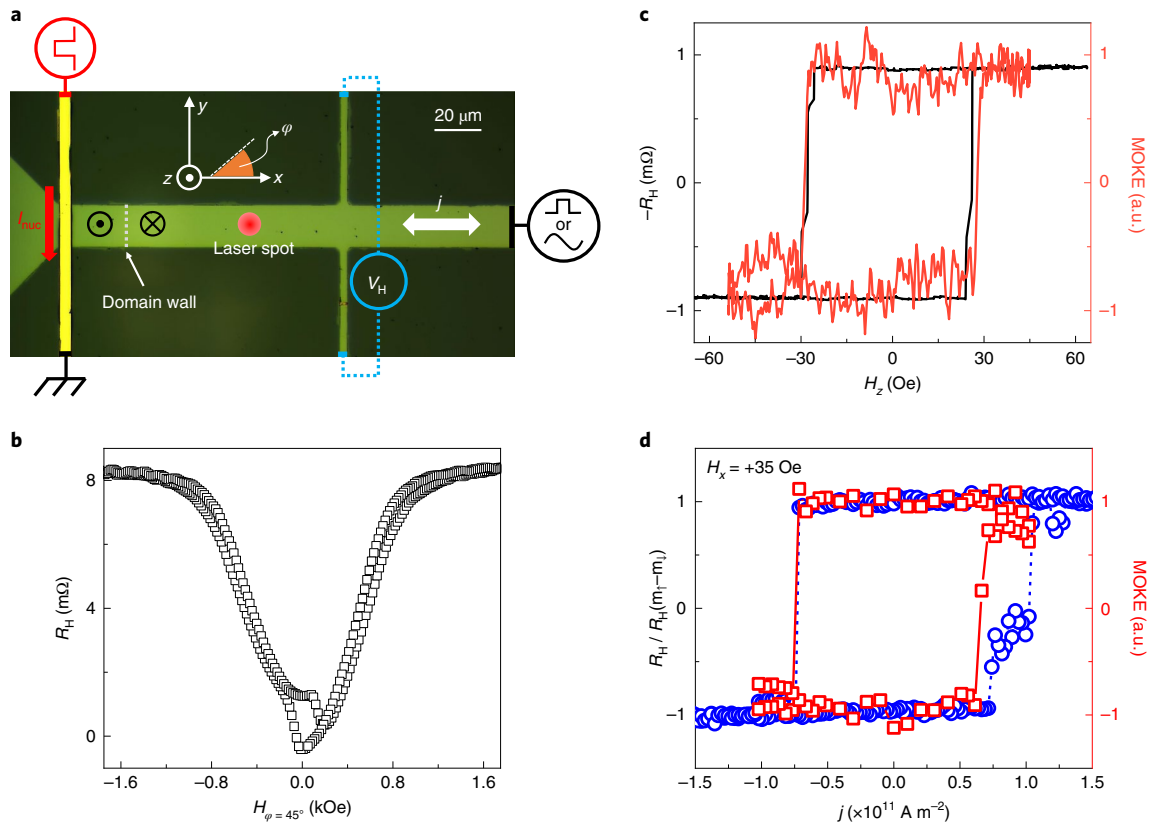


Fig. 1 | Experimental set-up and current-induced magnetization reversal. **a**, Optical micrograph of a DW track with schematically indicated electrical connections and definition of the coordinate system and in-plane angle. The black region is the substrate, the light green region is the TmIG/Pt bilayer track, and the vertical bright yellow line is the DW nucleation wire. Thick red and white arrows show the direction of the nucleation (I_{nuc}) and DW drive currents. A schematic depiction of the domain configuration is shown near the nucleation wire after injection of I_{nuc} for magnetization initially saturated along $-z$. **b**, Hall resistance R_H measured while sweeping an in-plane field (H) at $\varphi_H = 45^\circ$, corresponding to the spin Hall magnetoresistance. **c**, Out-of-plane hysteresis loop measured using the anomalous Hall-like signal (black curve) and the MOKE measured near the centre of the track. **d**, Current-induced switching probed electrically (through R_H) and by MOKE.

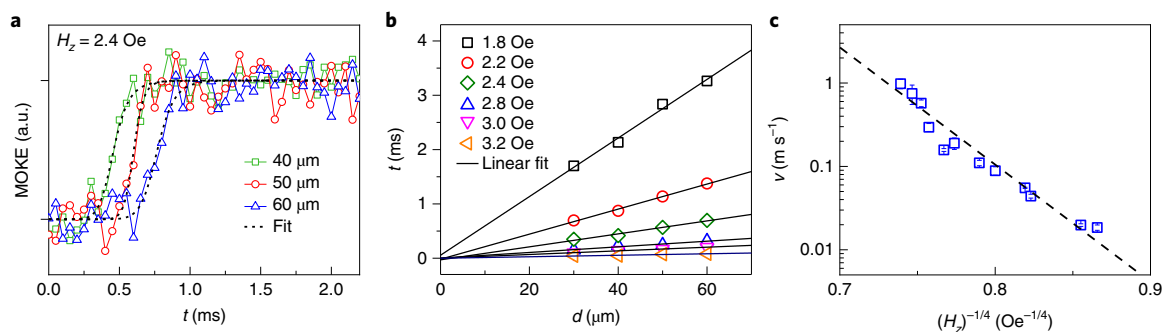


Fig. 2 | Field-driven DW dynamics. **a**, Time-resolved MOKE reversal transients measured at several distances from the Au nucleation wire, for a driving field of $H_z = 2.4$ Oe, fitted by an error function to determine the mean DW arrival time. The magnetization was first saturated along the $-z$ direction and then an out-of-plane driving field H_z below the coercive field was applied. A short current pulse was then injected along the Au wire at time $t = 0$ such that the local Oersted field nucleates a reverse domain, which expands under H_z . The MOKE signal was monitored at a distance d from the nucleation line to detect passage of the propagating DW. **b**, DW arrival time versus position, extracted by fitting the MOKE transients with an error function, with $d = 0$ corresponding to the position of the Au nucleation line, along with linear fits whose slope is used to extract the mean velocity. **c**, DW velocity v as a function of driving field H_z plotted for creep scaling. A small field offset from the Earth's magnetic field was determined by comparing measurements at positive and negative H_z and was used to correct the driving field plotted in the horizontal axis. Error bars were computed based on the error in the linear fits shown in **b**.

DW velocity v follows the usual creep scaling $\ln v \propto H_z^{-1/4}$ in this low-field regime (Fig. 2c), indicating propagation through a weak disorder potential.

We quantified the current-induced effective field acting on DWs by measuring its influence on DW propagation¹². The current-induced effective field manifests as a variation in the DW propagation

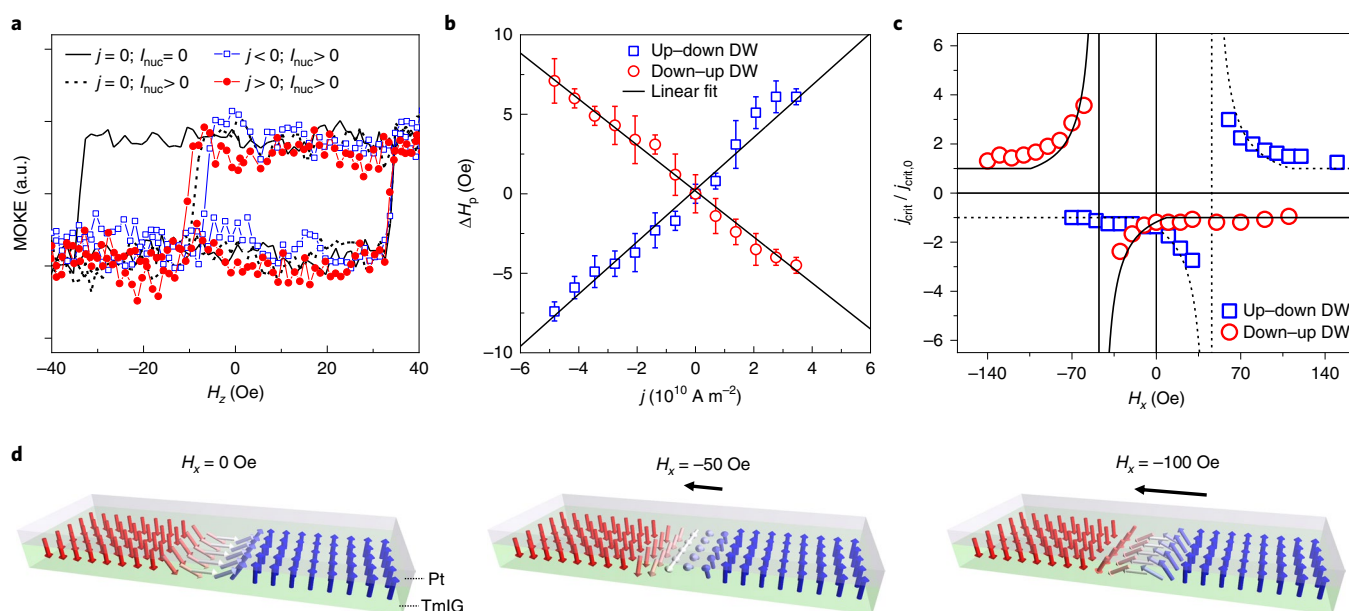


Fig. 3 | Current-assisted depinning and DW propagation. **a**, MOKE signal in the absence (continuous black line) and presence (dashed black line) of nucleation pulses injected along the Au nucleation line at the zero-field crossing of the positive-going field sweep half-cycle. The influence of positive (red curve) and negative (blue curve) current injection along the track (current density j) after domain nucleation. The magnetization switching that occurs at around $H_z \sim 30$ Oe corresponds to domain nucleation, whereas the switching around $H_z \sim -10$ Oe corresponds to DW propagation. **b**, Change in DW propagation field (ΔH_p) as a function of j , for up-down and down-up DW. Error bars represent the uncertainty in estimating the switching field given the finite signal-to-noise ratio of the MOKE signal. **c**, Critical current (j_{crit}) normalized by the critical current obtained at $H_x = 0$ Oe, for DW depinning for up-down and down-up DWs as a function of in-plane field H_x . Error bars were computed by repeating each measurement five times and computing the s.d., and are approximately the size of the symbols used in the figure and so are omitted. **d**, Schematic representation of the behaviour of a Dzyaloshinskii-Moriya stabilized Néel DW in the presence of an increasing field H_x oriented antiparallel to its internal moment.

field H_p under d.c. current injection^{12,30}. H_p was extracted from hysteresis loops (Fig. 3a) in which DWs were controllably nucleated during one half of the field-sweep cycle, such that the switching field corresponds to the field required to depin the nucleated DW. The linear relative change in the propagation field $\Delta H_p \propto j$ (Fig. 3a,b) indicates that the current generates an effective out-of-plane field $|H_{eff}/j| \approx 15.5 \pm 1.2$ Oe per 10^{11} A m $^{-2}$, which assists DW propagation in the direction of electron flow. This result is in quantitative agreement with harmonic measurements of the damping-like torque (see Supplementary Information).

Damping-like torque manifests as a z -axis effective field $H_{eff} = \frac{\pi}{2} H_{DL} \cos(\psi)$ in a DW, where ψ is the angle between the DW moment and the x axis. Figure 3b hence implies that the DWs are Néel type ($\psi = 0, \pi$) and that up-down and down-up DWs have oppositely oriented moments because H_{eff} is of opposite sign. This suggests a chiral exchange field H_{DMI} that stabilizes homochiral Néel DWs in this system. To confirm this, we measured the dependence of the critical depinning current j_{crit} on the longitudinal field H_x (see Methods). j_{crit} represents the threshold at which H_{eff} overcomes the effective pinning field, and it should hence vary with ψ . Figure 3c shows that for down-up DWs, j_{crit} is unchanged for $H_x > 0$, diverges near $H_x \sim -50$ Oe, and changes sign across this threshold. Up-down DWs exhibit similar behaviour, with the signs of j and H_x inverted. This can be understood from the schematics in Fig. 3d. For down-up walls, the DW moment orients to the right at zero field and rotates from Néel to Bloch to Néel with opposite chirality under increasing $H_x < 0$. H_{eff} has opposite signs for oppositely oriented Néel DWs and vanishes for Bloch DWs, leading to the observed behaviour of j_{crit} versus H_x . As shown in Fig. 3c, the data are well fitted by a simple model in which j_{crit} scales as $1/H_{eff}$ and ψ follows the usual one-dimensional DW model³⁰. We find a chiral exchange field $|H_{DMI}| \approx 47$ Oe corresponding to an interfacial DMI constant

$|D| \approx 0.002$ mJ m $^{-2}$ (see Supplementary Information). Normalized to the film thickness, D is nearly two orders of magnitude lower than in Pt/metallic-ferromagnet systems. However, because the threshold DMI strength (D^{th}) required to stabilize Néel DWs³¹ scales as the DW demagnetizing energy, $|D^{th}| = (2t \ln(2)/\pi^2)\mu_0 M_s^2$ (where t is the magnetic layer thickness), the threshold required for Néel DWs in these low- M_s garnets is a factor of $\sim 10^2$ smaller than that of a 1-nm-thick Co film.

Pt is known to induce a strong DMI at Pt/ferromagnetic-metal interfaces, but the chirality in all previously studied systems is left-handed when the Pt layer is underneath the ferromagnetic metal, that is, on the substrate side³². Surprisingly, the DWs in this system are also left-handed despite the fact that Pt is on top of the magnetic layer, meaning that they have the opposite chirality relative to that induced by Pt in all previously studied systems. This is evidenced by the in-plane field dependence in Fig. 3 and the fact that DWs move in the electron flow direction, opposite to that in metallic systems such as Pt/Co. To gain more insight into the origin of the chiral effective field, we varied the rare-earth ion in the garnet and the interface between the garnet and the Pt. Figure 4 shows ΔH_p versus j , measured as in Fig. 3a,b, for up-down DWs in TmIG/Pt, TbIG/Pt and TbIG/Cu(2 nm)/Pt under various H_x . We see that in all cases DWs move against current flow at zero H_x , and under $H_x > 0$ the slope of ΔH_p versus j inverts. This implies that all three systems share the same chirality with similar H_{DMI} strength, since the field at which H_{eff} vanishes and DWs become Bloch is similar. We finally estimate $|D| \approx 0.0014$ mJ m $^{-2}$ for the TbIG samples which, scaled by thickness, implies nearly the same interfacial DMI energy as for TmIG (see Supplementary Information). In this case, there is no measurable change in the chiral exchange field.

If Pt were responsible for the interfacial DMI, then inserting a Cu spacer should significantly decrease its strength. A comparison

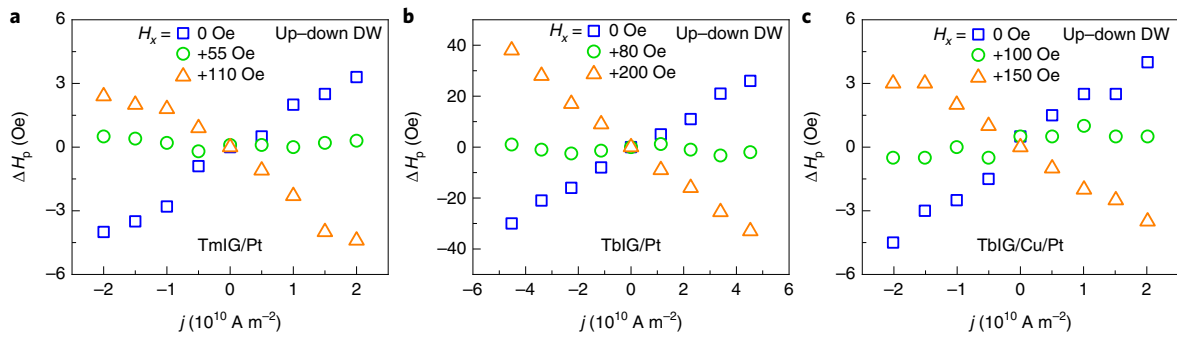


Fig. 4 | Measuring chiral exchange fields for various rare-earth garnets and interfaces. a–c, Measurement of the change in DW propagation fields as a function of current density j , similar to the measurement in Fig. 3b, for TmIG(5.1 nm)/Pt(4 nm) (**a**), TblG(7.1 nm)/Pt(4 nm) (**b**) and TblG(7.1 nm)/Cu(2 nm)/Pt(4 nm) (**c**). Measurements shown are for the case of an up-down DW, under zero applied field, with an applied field H_x that reduces the slope to zero (corresponding to the DMI effective field), and for a larger positive H_x that reorients the Néel DW to the opposite chirality, inverting the slope.

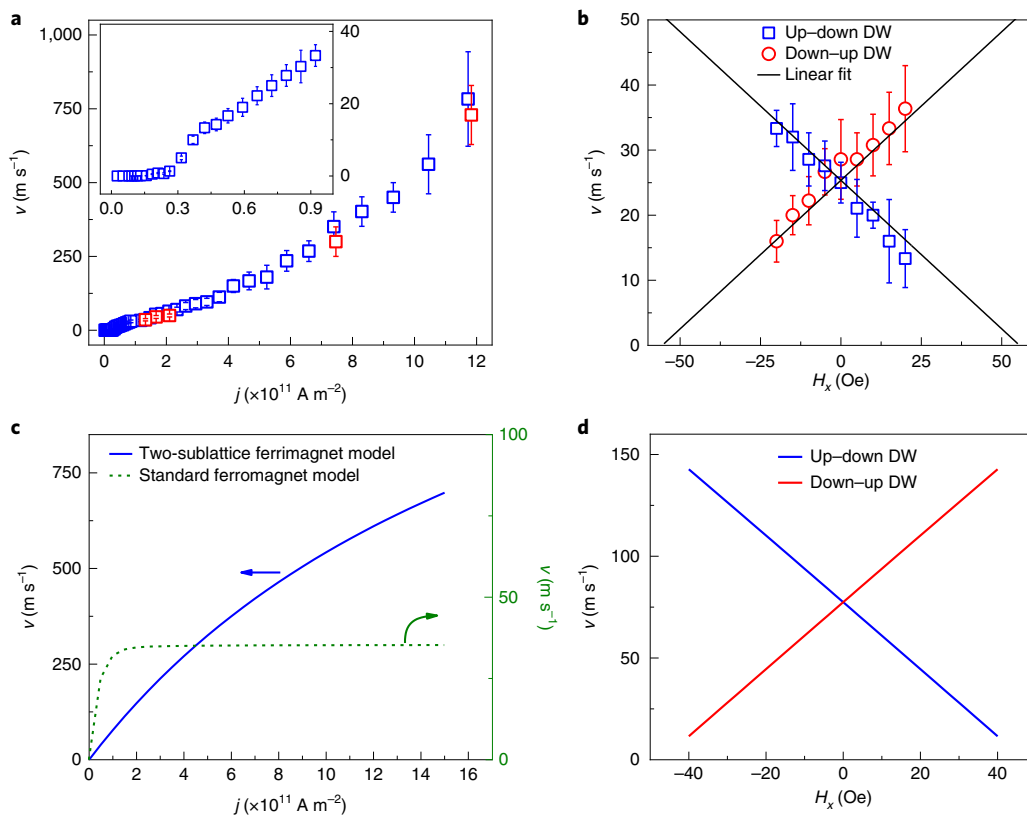


Fig. 5 | Current-driven DW velocity. a, DW velocity v versus current density j for TmIG/Pt. Inset, the region around the critical depinning threshold. Blue and red data points correspond to independent measurements on two different devices fabricated from the same film. **b,** Plot of v versus H_x measured at a current density of $j = 1 \times 10^{11} \text{ A m}^{-2}$ for up-down and down-up DWs. Linear fits extrapolated to $v = 0$ yield the DMI effective field. Error bars were computed from the error in the DW transit times between two MOKE probe points, based on the uncertainty of an error function fit to the MOKE reversal transients. **c,** Model calculations of v versus j in the case of a two-sublattice ferrimagnet model (left y axis) and a standard ferromagnetic model (right y axis). Quasi-linear non-saturating velocities are found in the former, whereas in the latter the velocity increases initially and quickly saturates around $j \sim 1.5 \times 10^{11} \text{ A m}^{-2}$. **d,** Model calculations of v versus H_x with a fixed current density of $j = 1 \times 10^{11} \text{ A m}^{-2}$ in the case of a two-sublattice ferrimagnet model for up-down and down-up DWs. See text for details regarding the model and parameters used.

between Fig. 3b and Fig. 3c shows that this is not the case. It is known from previous works that adding even a few ångström dusting layer between Pt and the ferromagnet is sufficient to entirely quench the interfacial DMI^{11,24}. The observation that insertion of 2 nm of Cu between Pt and the TmIG produces no measurable change in the DMI indicates strongly that it is not induced by the

Pt. The fact that the 2 nm Cu layer does change dramatically the damping-like torque at this interface in our experiment confirms that it is thick and continuous enough to change the nature of the interface itself. On the other hand, if bulk-like contributions played a role, one may expect a dependence on the heavy rare-earth ion, whose orbital moment is different for Tm and Tb, but this also is not

observed. Moreover, cycloidal order (Néel textures) requires a form of DMI associated with broken inversion symmetry at a surface, not in the bulk¹⁷. Because the DMI is insensitive to the top interface and occurs generally in these rare-earth garnets, the substrate oxide–magnetic oxide interface may instead play the dominant role. Rashba splitting is known to manifest at oxide–oxide interfaces^{2,33} such as LaAlO₃/SrTiO₃, which exhibit a variety of emergent two-dimensional magnetic phenomena⁴. The Rashba-generated DMI has recently been predicted at oxide–oxide interfaces^{3,34}, and the Rashba-induced DMI can occur even in materials lacking strong spin–orbit coupling²⁰. A more systematic study of the dependence of the DMI on garnet thickness, rare-earth ion, crystallographic orientation and substrate lattice mismatch could shed light into the origins of the interfacial DMI observed in this system.

Finally, we characterized high-speed DW dynamics driven by short current pulses (see Methods). Figure 5a shows DW velocity v as a function of j in TmIG/Pt. We observe velocities exceeding 800 m s⁻¹ at $j = 1.2 \times 10^{12}$ A m⁻², and a depinning threshold at $j \cong 0.4 \times 10^{11}$ A m⁻², which is about an order of magnitude lower than in polycrystalline metallic systems^{11,35,36}. Comparable speeds to those observed here have previously been reported in synthetic antiferromagnets³⁶ and metallic ferrimagnets at angular momentum compensation³⁷, but at significantly higher current densities. These results show that pure spin current from the spin Hall effect can drive homochiral DWs at very high speeds using modest current densities in insulating magnetic oxides.

Figure 5b shows that v varies linearly with H_x as expected for chiral Néel DWs driven by damping-like torque. The field at which the extrapolated velocity vanishes is ~ 50 Oe, which corresponds to H_{DMI} in agreement with our depinning measurements (Fig. 3). Hence, the DMI plays a critical role in the current-driven DW dynamics; however, the fast velocities cannot be accounted for by the DMI strength alone. In ferromagnets, DWs driven by damping-like spin–orbit torque exhibit a maximum velocity proportional to the DMI strength, which for the present material parameters (see Methods) would correspond to just a few tens of m s⁻¹ (Fig. 5c). However, for ferrimagnets, antiferromagnetic coupling of the sublattices leads to an inhibition of the DW plane precession that is responsible for the velocity saturation^{36,37}. As described in ref. ³⁷, in ferromagnets, the DW velocity can be written as $v(j) = \frac{\pi\gamma\Delta}{2\alpha} H_{\text{DL}} / \sqrt{(1 + (H_{\text{DL}}/\alpha H_{\text{DMI}})^2)}$, which tends to saturate for $H_{\text{DL}} \sim \alpha H_{\text{DMI}}$ with damping-like effective field $H_{\text{DL}} \propto j$ and DMI effective field $H_{\text{DMI}} \propto D$. For ferrimagnets, the DW dynamics can be accurately modelled by rescaling the gyromagnetic ratio γ and damping constant α to yield an equation of motion for the Néel vector, which takes into account the collective dynamics of two antiparallel sublattices. Following that approach (see Methods), we predict a qualitatively similar dynamics (Fig. 5c,d) to what we observe experimentally, showing that despite the relatively weak DMI, very fast DW speeds can be attained. In particular, since α is rescaled by a factor $\left(\frac{M_{s,1}}{\gamma_1} + \frac{M_{s,2}}{\gamma_2}\right) / \left(\frac{M_{s,1}}{\gamma_1} - \frac{M_{s,2}}{\gamma_2}\right) \approx 500$ for these material parameters (where the subscripts refer to the antiparallel sublattices; see Methods), much higher velocities can be attained because velocity saturation occurs at a much higher current density. Moreover, this implies that by tuning, for example, α it is possible to further increase the DW velocity at a given current density.

In conclusion, we report a chiral exchange field in centrosymmetric thin-film rare-earth iron garnets that stabilizes Néel DWs with a fixed chirality. We show that spin currents generated by charge current in an adjacent Pt layer can be used to exert substantial damping-like torque on these DWs, leading to efficient current-induced motion at zero applied field. We find small critical currents of a few 10^{10} A m⁻², which we attribute to the high-quality crystalline nature of these materials leading to a low density of defects.

Combined with a high current-driven mobility enabled by antiferromagnetic spin dynamics, this allows for fast DW motion at modest current densities, with speeds ~ 800 m s⁻¹ per $j \cong 1.2 \times 10^{12}$ A m⁻². These attributes make rare-earth iron garnets promising for low-power, high-speed DW motions. We find that the interfacial DMI persists whether Pt is in direct contact with the film or not, and occurs generally in a family of rare-earth garnets, and we suggest that it may originate at the substrate oxide–oxide interface via a Rashba-type spin–orbit interaction. The possibility to achieve chiral magnetism in magnetic insulators and efficient manipulation of chiral textures by pure spin currents marks an important advance in oxide-based spin-orbitronics. Note added in proof: After submission of this manuscript we became aware of another study by Vélez et al. reporting similar results in TmIG/Pt (ref. ³⁸).

Online content

Any methods, additional references, Nature Research reporting summaries, source data, statements of data availability and associated accession codes are available at <https://doi.org/10.1038/s41565-019-0421-2>.

Received: 29 October 2018; Accepted: 6 March 2019;

Published online: 01 April 2019

References

1. Yamada, H. et al. Engineered interface of magnetic oxides. *Science* **305**, 646–648 (2004).
2. Caviglia, A. D. et al. Tunable Rashba spin–orbit interaction at oxide interfaces. *Phys. Rev. Lett.* **104**, 126803 (2010).
3. Banerjee, S., Erten, O. & Randeria, M. Ferromagnetic exchange, spin–orbit coupling and spiral magnetism at the LaAlO₃/SrTiO₃ interface. *Nat. Phys.* **9**, 626–630 (2013).
4. Bhattacharya, A. & May, S. J. Magnetic oxide heterostructures. *Annu. Rev. Mater. Res.* **44**, 65–90 (2014).
5. Bibes, M. & Barthélémy, A. Oxide spintronics. *IEEE Trans. Electron. Dev.* **54**, 1003–1023 (2007).
6. Kajiwara, Y. et al. Transmission of electrical signals by spin-wave interconversion in a magnetic insulator. *Nature* **464**, 262–266 (2010).
7. Chumak, A. V., Vasyuchka, V. I., Serga, A. A. & Hillebrands, B. Magnon spintronics. *Nat. Phys.* **11**, 453–461 (2015).
8. Nakayama, H. et al. Spin Hall magnetoresistance induced by a nonequilibrium proximity effect. *Phys. Rev. Lett.* **110**, 206601 (2013).
9. Cornelissen, L. J., Liu, J., Duine, R. A., Youssef, J. B. & Van Wees, B. J. Long distance transport of magnon spin information in a magnetic insulator at room temperature. *Nat. Phys.* **11**, 1022–1026 (2015).
10. Avci, C. O. et al. Current induced switching in a magnetic insulator. *Nat. Mater.* **16**, 309–314 (2017).
11. Ryu, K., Thomas, L., Yang, S. & Parkin, S. Chiral spin torque at magnetic domain walls. *Nat. Nanotechnol.* **8**, 527–533 (2013).
12. Emori, S., Bauer, U., Ahn, S.-M., Martinez, E. & Beach, G. S. D. Current-driven dynamics of chiral ferromagnetic domain walls. *Nat. Mater.* **12**, 611–616 (2013).
13. Torrejon, J. et al. Interface control of the magnetic chirality in CoFeB/MgO heterostructures with heavy-metal underlayers. *Nat. Commun.* **5**, 4655 (2014).
14. Mühlbauer, S. et al. Skyrmion lattice in a chiral magnet. *Science* **323**, 915–919 (2009).
15. Yu, X. Z. et al. Near room-temperature formation of a skyrmion crystal in thin-films of the helimagnet FeGe. *Nat. Mater.* **10**, 106–109 (2011).
16. Seki, S., Yu, X. Z., Ishiwata, S. & Tokura, Y. Observation of skyrmions in a multiferroic material. *Science* **336**, 198–201 (2012).
17. Bode, M. et al. Chiral magnetic order at surfaces driven by inversion asymmetry. *Nature* **447**, 190–193 (2007).
18. Thiaville, A., Rohart, S., Jue, E., Cros, V. & Fert, A. Dynamics of Dzyaloshinskii domain walls in ultrathin magnetic films. *Eur. Lett.* **100**, 57002 (2012).
19. Fert, A., Cros, V. & Sampaio, J. Skyrmions on the track. *Nat. Nanotechnol.* **8**, 152–156 (2013).
20. Yang, H. et al. Significant Dzyaloshinskii–Moriya interaction at graphene–ferromagnet interfaces due to the Rashba effect. *Nat. Mater.* **17**, 605–609 (2018).
21. Woo, S. et al. Observation of room-temperature magnetic skyrmions and their current-driven dynamics in ultrathin metallic ferromagnets. *Nat. Mater.* **15**, 501–506 (2016).
22. Boulle, O. et al. Room-temperature chiral magnetic skyrmions in ultrathin magnetic nanostructures. *Nat. Nanotechnol.* **11**, 449–454 (2016).

23. Jiang, W. et al. Blowing magnetic skyrmion bubbles. *Science* **349**, 283–286 (2015).
24. Ryu, K., Yang, S., Thomas, L. & Parkin, S. S. P. Chiral spin torque arising from proximity-induced magnetization. *Nat. Commun.* **5**, 3910 (2014).
25. Matsuno, J. et al. Interface-driven topological Hall effect in SrRuO₃-SrIrO₃ bilayer. *Sci. Adv.* **2**, e1600304 (2016).
26. Ohuchi, Y. et al. Electric-field control of anomalous and topological Hall effects in oxide bilayer thin film. *Nat. Commun.* **9**, 213 (2018).
27. Wang, L. et al. Ferroelectrically tunable magnetic skyrmions in ultrathin oxide heterostructures. *Nat. Mater.* **17**, 1087–1094 (2018).
28. Kan, D., Moriyama, T., Kobayashi, K. & Shimakawa, Y. Alternative to the topological interpretation of the transverse resistivity anomalies in SrRuO₃. *Phys. Rev. B* **98**, 180408(R) (2018).
29. Gerber, A. Interpretation of experimental evidence of the topological Hall effect. *Phys. Rev. B* **98**, 214440 (2018).
30. Emori, S. et al. Spin Hall torque magnetometry of Dzyaloshinskii domain walls. *Phys. Rev. B* **90**, 184427 (2014).
31. Lemesh, I., Büttner, F. & Beach, G. S. D. Accurate model of the stripe domain phase of perpendicularly magnetized multilayers. *Phys. Rev. B* **95**, 174423 (2017).
32. Heide, M. & Bihlmayer, G. Dzyaloshinskii–Moriya interaction accounting for the orientation of magnetic domains in ultrathin films: Fe/W(110). *Phys. Rev. B* **78**, 140403(R) (2008).
33. Veit, M. J., Arras, R., Ramshaw, B. J., Pentcheva, R. & Suzuki, Y. Nonzero Berry phase in quantum oscillations from giant Rashba-type spin splitting in LaTiO₃/SrTiO₃ heterostructures. *Nat. Commun.* **9**, 1458 (2018).
34. Banerjee, S., Rowland, J., Erten, O. & Randeria, M. Enhanced stability of skyrmions in two-dimensional chiral magnets with Rashba spin–orbit coupling. *Phys. Rev. X* **4**, 031045 (2014).
35. Miron, I. M. et al. Fast current-induced domain-wall motion controlled by the Rashba effect. *Nat. Mater.* **10**, 419–423 (2011).
36. Yang, S., Ryu, K. & Parkin, S. Domain-wall velocities of up to 750 m s⁻¹ driven by exchange-coupling torque in synthetic antiferromagnets. *Nat. Nanotechnol.* **10**, 221–226 (2015).
37. Caretta, L. et al. Fast current-driven domain walls and small skyrmions in a compensated ferrimagnet. *Nat. Nanotechnol.* **13**, 1154–1160 (2018).
38. Vélaz, S. et al. High-speed domainwall racetracks in a magnetic insulator. Preprint at <https://arxiv.org/abs/1902.05639> (2019).

Acknowledgements

This work was supported by the DARPA TEE program. The authors thank L. Liu for use of ion milling equipment. C.O.A. thanks A. Jun Tan for discussions.

Author contributions

C.O.A., C.A.R. and G.S.D.B. conceived the project and planned the experiments. E.R. synthesized and characterized the TmIG and TbIG samples. C.O.A. deposited the metal layers and micro-fabricated the domain wall tracks. C.O.A., L.C., M.M., C.M. and D.B. prepared the experimental set-up. C.O.A. and L.C. performed the measurements. L.C. and F.B. modelled the domain wall dynamics. C.O.A. and G.S.D.B. analysed the data and wrote the manuscript. All authors contributed to the discussion of the data in the manuscript and Supplementary Information.

Competing interests

The authors declare no competing interests.

Additional information

Supplementary information is available for this paper at <https://doi.org/10.1038/s41565-019-0421-2>.

Reprints and permissions information is available at www.nature.com/reprints.

Correspondence and requests for materials should be addressed to G.S.D.B.

Publisher's note: Springer Nature remains neutral with regard to jurisdictional claims in published maps and institutional affiliations.

© The Author(s), under exclusive licence to Springer Nature Limited 2019

Methods

Materials growth, characterization and device patterning. TmIG (5.1 nm) and TbIG (7.1 nm) films were deposited on $\text{Gd}_3\text{Ga}_5\text{O}_{12}$ (111) single-side-polished substrates by pulsed laser deposition using a 248 nm KrF excimer laser with 10 Hz repetition rate. The targets were prepared from Fe_2O_3 and Tm_2O_3 or Tb_2O_3 powder by a mixed oxide sintering method. Before and during deposition, the substrate holder was heated to a setpoint temperature of 900 °C, corresponding to a substrate temperature of 650 °C, in an oxygen atmosphere of 150 mtorr. The target-sample distance was 8 cm and the cooling rate of the chamber after deposition was 10 °C min⁻¹. These conditions yield films with an excess of rare-earth (RE:Fe of ~0.7) and the TbIG compensation temperature is ~330 K, higher than bulk (~250 K). The origin of this discrepancy may be off-stoichiometry and/or antisite defects and ions in valence states other than 3+, which changes the magnetization on the sublattices. This would lead to ionic site disorder (for example, Tb^{3+} is known to transition to Tb^{4+} , a stable 4f ion, to enter octahedral sites), creating an imbalance between the sublattices compared to ideal TbIG. Epitaxial growth of the films was confirmed via a high-resolution X-ray diffraction 2θ - ω scan of the (444) reflection. Film thicknesses were determined by X-ray reflectometry. Atomic force microscopy measurements indicated a root-mean-square roughness of less than 1 nm taken over a 1 μm^2 area for all used samples.

The films have a perpendicular easy axis due to magnetoelastic anisotropy arising from epitaxial growth on the $\text{Gd}_3\text{Ga}_5\text{O}_{12}$ substrate. TmIG is under in-plane tensile strain with a negative magnetostriction coefficient λ_{111} ; TbIG is under in-plane compression with a positive λ_{111} . The room-temperature saturation magnetizations of the TmIG and TbIG films were 60 and 20 emu cm⁻³, respectively, measured using vibrating sample magnetometry. The effective perpendicular anisotropy field was determined from the field required to saturate the in-plane magnetization in SMR measurements (Fig. 1b), and corresponded to ~1 kOe for the TmIG film. The SMR signal did not saturate for TbIG for in-plane fields up to 20 kOe due to its higher perpendicular anisotropy field near the compensation temperature.

Metallic overlayers (Pt and Cu/Pt) were deposited by d.c. magnetron sputtering at room temperature with a base pressure < 3×10^{-7} torr and a deposition rate of ~2 nm min⁻¹. Film thicknesses were determined using a calibrated deposition rate.

Standard photolithography followed by Ar⁺ ion milling was used to define micrometre-sized DW track mesa structures with varying widths (10–80 μm) and lengths (50–200 μm). The contact pads and the nucleation wire were defined in a second lithography step followed by Ta(5 nm)/Au(60 nm) deposition and liftoff.

Electrical set-up and measurements. The Hall effect measurements reported in Fig. 1 were performed on 20- μm -wide and 200- μm -long devices by injecting an a.c. current with amplitude $I_{\text{rms}} = 2$ mA and frequency $\omega/2\pi = 3,678$ Hz and measuring the Hall voltage V_{ω} using a lock-in amplifier. The typical device resistance was ~1 k Ω . The measured a.c. Hall voltage was converted to a Hall resistance using $R_{\text{H}} = \frac{V_{\omega}}{I}$. Current-induced switching in Fig. 1d was characterized using a procedure similar to that in ref. 10. Briefly, we first saturated the film and then applied a large reverse field step to determine the full-scale change in either R_{H} or the MOKE signal upon magnetization reversal, which was used as a reference. Then, to generate the hysteresis loops shown, for the positive-going branch, we saturated the film in the -z direction and injected a 5 ms current pulse with a progressively increasing amplitude, and normalized the change in R_{H} or MOKE signal to the full-scale value to determine the fractional change in out-of-plane magnetization at each current data point. The negative-going branch was obtained similarly after saturating in the +z direction. Each data point represents switching obtained by analysing a signal-averaged switching transient obtained from five switching cycles for the Hall effect measurement and 1,000 switching cycles for the MOKE measurement, due to the lower signal-to-noise ratio for the latter.

MOKE. The MOKE set-up is in the polar configuration where the signal is related to the out-of-plane component of the magnetization, and the incident beam is normal to the sample plane. The light source is a continuous-wave diode laser with a wavelength of 632 nm, focused with a $\times 10$ objective and positioned relative to the sample using a high-resolution scanning stage. The laser spot size was determined using a knife-edge technique by scanning it over the edge of a lithographically defined Pt pad and fitting the measured reflectivity profile to an error function. The laser spot had a 1/e full width of 4.9 μm . Due to the low signal-to-noise ratio, MOKE switching measurements were obtained by signal-averaging on the order of 1,000 reversal transients.

Field/current-induced DW propagation. To determine the field-induced DW velocity, the magnetization was first saturated along the -z (+z) direction, then an out-of-plane driving field $+H_z$ ($-H_z$) below the coercive field was applied. A short current pulse (I_{nuc}) was injected along the Au wire at time $t = 0$ such that the local Oersted field nucleated a reverse domain, which expanded under H_z . The MOKE signal was monitored at a distance d from the nucleation line to detect passage of the propagating DW (Fig. 2a). For the current-induced DW propagation we nucleated a reverse domain by applying I_{nuc} along the nucleation wire, then sent current pulses of variable amplitude along the track to move the DW. To determine the DW speed reported in Fig. 5, we injected a series of short current pulses to drive it along the track and across the MOKE probing laser spot. The driving sequence was repeated at two probing positions and the velocity was taken as the ratio of the distance between the two locations and the cumulative pulse injection time between switching measured at the two locations.

Critical current measurements. The measurements of critical current j_{crit} versus in-plane field H_x in Fig. 3c were obtained as follows. For up-down DWs, a reversed domain was prepared as explained above. The MOKE spot was placed along the track away from the Au nucleation line, and a 70 μs current pulse was injected in the presence of a bias field H_x while the MOKE signal was recorded. The current amplitude of the pulse was progressively increased until switching was observed, and this threshold current was taken as the switching current. We then determined whether the same current density was capable of switching the local magnetization in the absence of initial domain nucleation, which would imply that reversal was through current-induced spin-orbit torque switching rather than DW propagation. Such data points were excluded from the data plotted in Fig. 3c, so those data represent current-driven depinning thresholds rather than current-induced switching.

Model calculations and simulation parameters. We numerically solved the 1D model of spin-orbit torque-driven DW motion for the case of a ferromagnet, and for a ferrimagnet in the case of strongly coupled (fully antiparallel) sublattices, following the model described in ref. 26. We set the sublattice magnetizations to $M_{s,1} = 3.3 \times 10^5$ A m⁻¹ (tetrahedral Fe³⁺ sublattice) and $M_{s,2} = 2.7 \times 10^5$ A m⁻¹ (octahedral Fe³⁺ and Tm³⁺) respectively, based on the bulk site occupancies in TmIG, yielding a net $M_s = 6 \times 10^4$ A m⁻¹. We considered $\gamma_1 = 2$ for the tetrahedral Fe³⁺ sublattice and $\gamma_2 = 1.63$ for the average gyromagnetic ratio of the octahedral Fe³⁺ and Tm³⁺. We used $\alpha = 0.002$, DW width $\Delta = 27$ nm, and set $H_{\text{DMI}} = 4.7$ mT and $H_{\text{DL}} = 1.55$ mT per 1×10^{11} A m⁻², as determined experimentally. To model ferromagnetic DW dynamics, the following scaling was applied³⁷:

$$\gamma \rightarrow \gamma' = \frac{M_s}{S} \quad (1)$$

$$\alpha \rightarrow \alpha' = \frac{S_0}{S} \quad (2)$$

with

$$M_s = |M_{s,1} - M_{s,2}| \quad (3)$$

$$S = \left| \frac{M_{s,1}}{\gamma_1} - \frac{M_{s,2}}{\gamma_2} \right| \quad (4)$$

$$S_0 = \alpha_0 \left(\frac{M_{s,1}}{\gamma_1} + \frac{M_{s,2}}{\gamma_2} \right) \quad (5)$$

where subscripts denote sublattices.

Data availability

The data that support the findings of this study are available from the corresponding author upon reasonable request.